© AUG 2026 | IRE Journals | Volume 10 Issue 2 | ISSN: 2456-8880
DOI: https://doi.org/10.64388/IREV10I2-1722215

Thermal Performance Optimization of a Phase Change Material (PCM)-Based Thermal Energy Storage System

AYUSHH KUMAR[1], DR. RAGHVENDRA KUMAR KHEDLE[2]
[1]*M. Tech. Scholar, Department of Mechanical Engineering, Technocrats Institute of Technology, Bhopal, India*
[2]*Guide and HOD, Department of Mechanical Engineering, Technocrats Institute of Technology, Bhopal, India*

Abstract- ***The mismatch between the availability of thermal energy and demand for it is a principal obstacle to the wider adoption of solar-thermal and waste-heat-recovery systems. Latent heat thermal energy storage (LHTES) using phase change materials (PCMs) offers compact, near-isothermal storage, yet the organic PCMs that store energy well conduct it poorly (0.15–0.25 W/m·K), which throttles charging and discharging power. This study addresses that limitation through a combined numerical, experimental and data-driven optimization of a vertical shell-and-tube LHTES module charged by hot water. A commercial paraffin wax (measured melting range 40.2–44.1 °C, latent heat 178.4 kJ/kg) was characterised by differential scanning calorimetry. Two enhancement strategies—longitudinal copper fins and dispersion of aluminium-oxide nanoparticles—were investigated jointly rather than in isolation. A transient conjugate model using the enthalpy-porosity formulation with buoyancy-driven convection was developed in ANSYS Fluent, made grid- and time-step-independent, and validated against fifteen calibrated thermocouples to within 6.8%. A Box–Behnken design was expanded to 180 cases to train a 4-12-8-2 artificial neural network that predicts complete melting time and stored energy with a testing coefficient of determination of 0.9921. Coupling the surrogate to a non-dominated sorting genetic algorithm (NSGA-II) generated the melting-time–stored-energy Pareto front, from which a preferred design was selected by TOPSIS. The optimum—eight fins of 22.5 mm height with 2.0% nanoparticle loading at 70 °C inlet—reduced complete melting time from 218.0 to 74.6 min (a 65.8% reduction) for only a 4.1% loss of stored energy, raised average charging power from 62 to 173 W, and improved exergy efficiency from 41.2% to 52.7%. Fin geometry and nanoparticle loading interact sub-additively, and the nanoparticle benefit saturates near 2% by mass.***

Keywords: Phase Change Material, Latent Heat Thermal Energy Storage, Enthalpy-Porosity Method, Nano-Enhanced PCM, Multi-Objective Optimization

I. INTRODUCTION

Global primary-energy demand has continued to climb through the first quarter of the twenty-first century, and although the renewable share has grown, the transition has exposed a structural difficulty that is not one of generation capacity. Solar and wind resources are intermittent, and thermal loads in buildings and process industries rarely coincide in time with their availability [1]. A solar water heater delivers its greatest output around solar noon, whereas household demand peaks in the early morning and late evening. In each such case energy is available at one time and required at another, and the value of the resource depends on the ability to shift it. Thermal energy storage (TES) performs this shifting for heat, and several national roadmaps now identify storage, rather than generation, as the binding constraint on further decarbonisation of the heat sector [2].

Latent heat thermal energy storage (LHTES) exploits the enthalpy change of a solid-to-liquid transition. Because the enthalpy of fusion of common storage materials lies between 120 and 250 kJ/kg, whereas the sensible enthalpy stored in water over a 20 K rise is only about 84 kJ/kg, a latent store accommodates two to three times the energy of a sensible store of equal volume [3]. The transition also occurs over a narrow temperature interval, so the store charges and discharges at a nearly constant temperature—decisive where thermal quality matters.

The motivation for this work lies in the gap between that promise and the observed performance of real units. The materials that combine adequate latent heat, chemical stability, low cost and non-toxicity—principally the paraffins and fatty acids—are also poor conductors, with values of 0.15–0.25 W/m·K comparable to an insulating polymer [4]. As melting

proceeds inward from the heat-transfer surface, the growing liquid layer interposes an increasing thermal resistance between source and remaining solid, so that a store thermodynamically capable of accepting a large quantity of energy is kinetically incapable of accepting it quickly. Charging times of several hours are routinely reported for laboratory modules of only a few litres [5]; in a domestic solar application with a five-to-six-hour collection window, such a store never reaches full charge.

Research on heat-transfer enhancement in LHTES falls into a few families: extended surfaces such as fins; high-conductivity porous scaffolds; dispersion of conductive nanoparticles; encapsulation; and multiple-PCM cascades [6], [7]. Each has been studied extensively in isolation and each can deliver substantial improvement alone. What has been studied far less is the interaction between strategies and the correct allocation of design effort among them. Fins increase the effective heat-transfer area but displace PCM, and beyond a certain density they suppress the buoyancy-driven convection that would otherwise contribute to transport [8]. Nanoparticles raise effective conductivity but increase viscosity—again suppressing convection—and dilute the latent heat in proportion to their mass fraction [9]. There is therefore an optimum, rather than a monotonic trend, in each design variable, and its location depends on the others. This is precisely the situation in which a one-factor-at-a-time study misleads and a formal optimization framework is required.

The computational cost of transient phase-change simulation compounds the difficulty: a single three-dimensional charging run may take twenty to forty hours, and an exhaustive search over four variables at five levels each would demand 625 such runs. Surrogate modelling—training a cheap approximating model on a small designed set of high-fidelity simulations and then searching it exhaustively—offers a way out, and artificial neural networks (ANNs) are especially effective because they impose no functional form and handle the strong non-linearities of phase change [10], [11]. This paper combines validated high-fidelity simulation, statistically efficient experimental design and surrogate-assisted multi-objective optimization, in the conviction that doing so yields both better designs and a clearer understanding of why they are better. Section 2 reviews the literature; Section 3 identifies the research gap; Section 4 states the objectives; Section 5 details the methodology; Sections 6–9 present results, graphical and tabular findings and a comparative analysis; and Sections 10–11 conclude and outline future work.

II. LITERATURE REVIEW

Research relevant to the thermal enhancement of LHTES can be grouped under four headings: selection and characterisation of phase change materials; enhancement by extended surfaces; nano-enhanced PCMs; and numerical-modelling and optimization approaches. A comparative analysis of representative studies then yields the research gaps addressed here.

2.1 Selection and characterisation of phase change materials

The choice of storage medium fixes the operating band and constrains every later choice of container and enhancement technique. Rathore and Shukla [17] drew attention to discrepancies of up to ten per cent between supplier-quoted and DSC-measured latent heat, motivating independent characterisation of procured material. Paraffins dominate low-temperature duty: their melting point rises approximately linearly with carbon number, and their congruent melting and negligible supercooling have been confirmed over long cycling campaigns, with Rathod and Banerjee [18] reporting latent-heat degradation below three per cent after a thousand cycles. Fatty acids offer comparable latent heat but are mildly corrosive and odorous [19], while salt hydrates offer higher volumetric latent heat and conductivity but suffer incongruent melting and supercooling [20]. Representative properties are compiled in Table 1.

Table 1. Thermophysical properties of candidate PCMs reported in recent literature.

PCM	Melting range (°C)	Latent heat (kJ/kg)	Conductivity (W/m·K)	Family
n-Octadecane	27–29	243	0.148–0.358	Paraffin

Paraffin RT-42	38–43	165–180	0.20	Paraffin
Paraffin wax (technical)	40–44	170–190	0.21–0.24	Paraffin
Lauric acid	43–44	187	0.147–0.190	Fatty acid
Myristic acid	52–54	190	0.150	Fatty acid
Sodium sulphate decahydrate	32–33	254	0.544	Salt hydrate
Calcium chloride hexahydrate	29–30	190	0.540–1.088	Salt hydrate

2.2 Heat-transfer enhancement by extended surfaces

Extended surfaces are the oldest, cheapest and most robust means of augmenting heat transfer in an LHTES unit: a fin conducts heat from the tube wall deep into the PCM, shortening the conduction length and creating multiple simultaneously advancing melt fronts. Abdulateef et al. [22] found longitudinal fins superior to annular fins because they do not obstruct the vertical buoyancy-driven circulation. Fin number and dimensions involve a direct trade-off—each fin displaces PCM and closely spaced fins impede convective rolls. Mahdi et al. [23] reported melting time falling steeply as fin count rose from two to eight but only marginally beyond, and Deng et al. [24] identified an optimum fin height near seventy per cent of the annular gap. Fin thickness is generally least influential once fin efficiency is high, so it is commonly examined parametrically and fixed. Kirincic et al. [29] provided an experimental benchmark, reporting a 51% reduction in charging time, and their data are used for validation here (Table 2).

Table 2. Summary of representative fin-based enhancement studies (2020–2025).

Reference	Configuration	Principal variable	Reported improvement
Abdulateef et al. [22]	Triplex tube	Fin orientation	25–30% faster melting
Mahdi et al. [23]	Shell and tube	Fin number	62% at 8 fins
Deng et al. [24]	Shell and tube	Fin height	Optimum at 0.7 of gap
Tian et al. [26]	Enclosure	Topology-optimised fins	41% vs uniform fins
Zhang et al. [27]	Shell and tube	Graded fin length	22% vs uniform
Kirincic et al. [29]	Shell and tube	Experimental validation	51% charging reduction

2.3 Nano-enhanced phase change materials

Dispersing conductive nanoparticles to form a nano-enhanced PCM (NePCM) raises effective conductivity uniformly through the volume rather than concentrating it near a surface. Metal oxides such as Al_2O_3 and CuO are chemically stable and inexpensive, while carbon additives offer higher conductivity at lower density. Reported enhancements scatter considerably (Table 3), reflecting sensitivity to preparation and stabilisation. Critically, the optimum loading in a finned unit is lower than in an unfinned one, so the two enhancement variables must be treated jointly—a point that motivates the combined optimization pursued here.

Table 3. Summary of representative nano-enhanced PCM studies (2020–2025).

Reference	Nanoparticle	Loading	Conductivity gain	Melting-time reduction
Sharma et al. [31]	Al_2O_3	1–6 wt%	8–41%	Optimum near 4 wt%
Arici et al. [32]	CuO	1–4 wt%	12–34%	13% at 4 wt%
Rehman et al. [33]	Graphene	0.5–3 wt%	45–165%	38% at 3 wt%
Sarafraz et al. [34]	CNT	0.1–1.5 wt%	20–78%	26% at 1.5 wt%
Sheikholeslami et al. [36]	CuO + fins	4 wt%	33%	Combined 58%

2.4 Numerical modelling and optimization approaches

Solid–liquid phase change is a moving-boundary problem, and the fixed-grid enthalpy-porosity method of Voller and Prakash [40] is implemented in every major solver: total enthalpy is split into sensible and latent parts, and the mushy region is treated as a porous medium with a Darcy-type momentum sink driving velocity to zero as the liquid fraction vanishes. The mushy-zone constant is the principal empirical parameter; Fadl and Eames [41] found predicted melting times varying by more than twenty per cent across the common range and recommended treating it as a calibration parameter, which is done here. Natural convection must be retained through the Boussinesq approximation. On optimization, response-surface methodology using Box–Behnken designs supports ANOVA and captures curvature, but the quadratic form represents LHTES saturation only approximately. ANNs impose no functional form and achieve accuracy comparable to CFD uncertainty [43], [44]. Multi-objective optimization by NSGA-II generates the Pareto front directly, deferring the value judgement to a decision step [45]; coupling surrogates with evolutionary optimization has been applied to LHTES only recently [46], [47].

III. RESEARCH GAP IDENTIFICATION

Although both fins and nanoparticles have been studied extensively, the reviewed literature reveals persistent gaps. Fins and nanoparticles are almost always treated in isolation and never optimized jointly, despite acting on the same thermal resistance and interacting through convection. The capacity penalty accompanying a reduction in melting time is inconsistently reported, so net benefit cannot be judged. Multi-objective treatments exposing the power–capacity trade-off as a Pareto front are rare, and rarer still combined with a surrogate. Surrogate-derived optima are seldom verified experimentally, second-law (exergy) assessment is largely neglected even though enhancement alters the temperature at which energy is stored, and discharge performance is under-reported although solidification is conduction-dominated and often rate-limiting. This study is designed to close all six gaps.

IV. OBJECTIVES OF THE STUDY

The specific objectives pursued in this study are as follows:

1. To select and experimentally characterise a suitable organic PCM for a nominal operating temperature of 42 °C—determining its melting range, latent heat, specific heat and thermal stability—and to prepare and characterise nano-enhanced composites by dispersing Al_2O_3 nanoparticles at up to 3 wt%.
2. To design and fabricate a vertical shell-and-tube LHTES module (~2.5 L PCM) with an instrumented facility, and to develop a validated transient enthalpy-porosity model with natural convection that is grid- and time-step-independent.
3. To resolve the individual and interactive influence of fin number, fin height, nanoparticle mass fraction and heat-transfer-fluid inlet temperature on melting time, stored energy, charging power and exergy efficiency using a Box–Behnken design with ANOVA.

© AUG 2026 | IRE Journals | Volume 10 Issue 2 | ISSN: 2456-8880
DOI: https://doi.org/10.64388/IREV10I2-1722215

4. To train and validate an ANN surrogate, couple it to NSGA-II to obtain the melting-time–stored-energy Pareto front, select a preferred design by TOPSIS, and verify the optimum by high-fidelity simulation and experiment on both first-law and second-law bases.

V. METHODOLOGY

The methodology follows five sequential phases: (I) PCM selection, characterisation and nano-composite preparation; (II) module and facility design with development of a validated transient model; (III) parametric exercise of the model to establish the influence of each variable; (IV) a Box–Behnken campaign with regression fitting and ANN surrogate training; and (V) ANN-coupled NSGA-II optimization, TOPSIS selection and experimental/numerical verification. The complete workflow is summarised in Fig. 1.

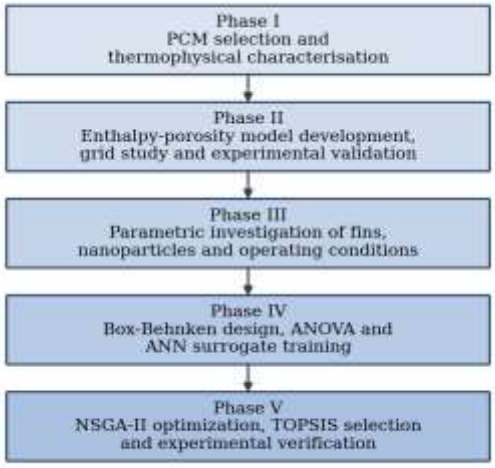

Fig. 1. Schematic of the five-phase research methodology adopted in the present work.

5.1 Storage module and materials

A vertical shell-and-tube configuration was adopted because it is the most widely used geometry in commercial low-temperature LHTES, permits fully developed buoyancy-driven convection and is readily parameterised. The heat-transfer fluid flows upward through a central copper tube; the PCM occupies the annulus between the tube and an outer acrylic shell that permits visual observation. Longitudinal copper fins of rectangular cross-section are brazed to the tube at uniform angular spacing. The 22 mm tube and 88 mm shell give a 33 mm annular gap, and the 500 mm active length gives 2.83 L of PCM (~2.47 kg, ~440 kJ latent capacity). Geometric specifications are listed in Table 4.

Table 4. Geometrical specifications of the LHTES module.

Parameter	Value	Parameter	Value
Inner tube outer diameter	22 mm	Fin number (range)	0, 4, 6, 8, 10, 12
Shell inner diameter	88 mm	Fin height (range)	10–25 mm
Annular gap	33 mm	Fin thickness (range)	0.5–2.5 mm
Active length	500 mm	PCM volume (unfinned)	2.83 L
PCM mass (unfinned)	2.47 kg	Nominal latent capacity	440 kJ

A commercial paraffin wax (nominal melting range 40–44 °C) was characterised by DSC on 8 mg samples at 5 K/min under nitrogen. The thermogram shows a principal endothermic peak with onset at 40.2 °C and maximum at 42.8 °C (Fig. 2); the measured latent heat was 178.4 kJ/kg, about six per cent below the supplier

© AUG 2026 | IRE Journals | Volume 10 Issue 2 | ISSN: 2456-8880
DOI: https://doi.org/10.64388/IREV10I2-1722215

value, and supercooling was below 1.5 K. Thermogravimetric analysis showed no mass loss below 180 °C. Measured properties are given in Table 5. Al_2O_3 nanoparticles (30 nm, 99.8% purity) were dispersed at 1.0, 2.0 and 3.0 wt% by the two-step method with surfactant and probe sonication; the 1 and 2 wt% composites showed no visible sedimentation over 72 h.

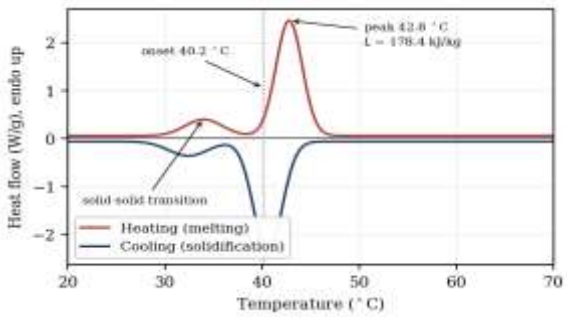

Fig. 2. DSC thermogram of the selected paraffin wax during heating and cooling.

Table 5. Measured thermophysical properties of the selected paraffin wax.

Property	Solid	Liquid	Unit
Solidus / liquidus temperature	40.2	44.1	°C
Latent heat of fusion	178.4	178.4	kJ/kg
Density	896	782	kg/m³
Specific heat capacity	2150	2410	J/kg·K
Thermal conductivity	0.24	0.19	W/m·K
Dynamic viscosity	—	0.0032	Pa·s
Thermal expansion coefficient	—	0.00085	1/K

5.2 Mathematical formulation and computational model

The liquid PCM is treated as Newtonian, incompressible and laminar (maximum Rayleigh number 3.4×10^6), with density constant except in the buoyancy term, where the Boussinesq approximation applies. The enthalpy-porosity formulation is used, with continuity, momentum and energy equations:

$$\nabla \cdot V = 0 \quad (1)$$

$$\rho[\partial V/\partial t + (V\cdot\nabla)V] = -\nabla p + \mu\nabla^2 V + \rho g\beta(T - T_{ref}) + S \quad (2)$$

$$\partial(\rho H)/\partial t + \nabla\cdot(\rho V H) = \nabla\cdot(k\nabla T) \quad (3)$$

$$S = A_{mush}[(1-\gamma)^2/(\gamma^3+\varepsilon)]V \quad (4)$$

The total enthalpy is $H = h + \gamma L$, where the liquid fraction γ varies linearly across the mushy interval, and the mushy-zone constant A_mush was calibrated against measured temperature histories to 1×10^5 kg/m³·s. Effective composite properties follow the mixture rule for density, heat capacity and latent heat, the Maxwell model for conductivity and the Brinkman model for viscosity. The equations were discretised by the finite-volume method and solved in ANSYS Fluent with PRESTO! pressure interpolation, SIMPLE coupling and second-order upwind schemes (Table 6). Grid independence over five meshes selected M3 (~342,600 cells, melting time within 0.7% of the finest mesh); a 0.1 s time step was adopted. Each 3-D simulation required twelve to twenty-two hours—the direct justification for the surrogate strategy (Table 7).

Table 6. Solver settings and discretisation schemes.

Setting	Selection	Setting	Selection
Solver	Pressure-based, transient	Pressure–velocity coupling	SIMPLE
Phase-change model	Enthalpy-porosity	Pressure interpolation	PRESTO!

Mushy-zone constant	1×10^5 kg/m³·s	Momentum / energy scheme	Second-order upwind
Buoyancy	Boussinesq	Transient formulation	First-order implicit

Table 7. Grid-independence results (eight-fin configuration).

Mesh	Cell count	Melting time (min)	Deviation (%)	Wall-clock (h)
M1	96,400	88.7	6.9	4.2
M2	184,200	85.1	2.5	7.8
M3 (adopted)	342,600	83.6	0.7	14.9
M4	618,900	83.2	0.2	27.3
M5	1,041,500	83.0	—	46.6

5.3 Design of experiments and surrogate optimization

Four design variables were carried into the formal optimization, with fin thickness fixed at 1.5 mm and flow rate at 1.5 LPM after parametric screening (Table 8). A 29-run Box–Behnken design was executed and augmented by Latin-hypercube sampling to 180 cases for surrogate training. A feedforward multilayer perceptron with a 4-12-8-2 architecture (tanh hidden activations, linear outputs) was trained by Levenberg–Marquardt with early stopping from twenty random initialisations. The trained network was coupled to NSGA-II (population 100, 200 generations, simulated-binary crossover, polynomial mutation), and a single preferred design was selected from the Pareto set by TOPSIS under equal weights, with sensitivity to the weighting examined. Uncertainty in derived quantities was propagated by root-sum-square, giving ±3.4% in melting time, ±5.4% in charging power and ±6.7% in exergy efficiency.

Table 8. Design variables and their levels.

Variable	Symbol	Unit	Low (−1)	Centre (0)	High (+1)
Fin number	N_f	—	4	8	12
Fin height	H_f	mm	10	17.5	25
Nanoparticle mass fraction	φ	%	0	1.5	3.0
HTF inlet temperature	T_in	°C	60	67.5	75

VI. RESULTS AND DISCUSSION

6.1 Model validation and baseline behaviour

fact The model reproduces the characteristic three-stage temperature history—steep sensible rise, phase-transition plateau, second steep rise—at every thermocouple location. It underpredicts melting time consistently by 5.8–6.8% (Table 9), the consistent sign pointing to an omitted physical effect, chiefly thermal contact resistance at the brazed fin–tube joint. Given the ±3.4% experimental uncertainty, agreement within 6.8% is satisfactory; the model was further verified against Kirincic et al. [29] to within 7.4%, confirming the agreement does not arise from compensating errors. The unenhanced module charged at 70 °C required 218.0 min to melt: conduction dominates the thin early melt layer, after which a buoyant recirculation develops and produces a strongly asymmetric front, leaving a stubborn solid wedge in the bottom outer corner (Fig. 3). This uneven distribution of difficulty is the central physical of the problem.

© AUG 2026 | IRE Journals | Volume 10 Issue 2 | ISSN: 2456-8880
DOI: https://doi.org/10.64388/IREV10I2-1722215

Table 9. Validation of the numerical model against experimental data.

Configuration	T_in (°C)	Measured t_m (min)	Predicted t_m (min)	Deviation (%)
No fins	65	246.5	231.8	−6.0
No fins	70	218.0	205.4	−5.8
No fins	75	191.2	179.6	−6.1
4 fins, 20 mm	70	132.4	123.4	−6.8
8 fins, 20 mm	70	96.3	90.6	−5.9
8 fins, 20 mm, 2 wt%	70	87.4	82.1	−6.1

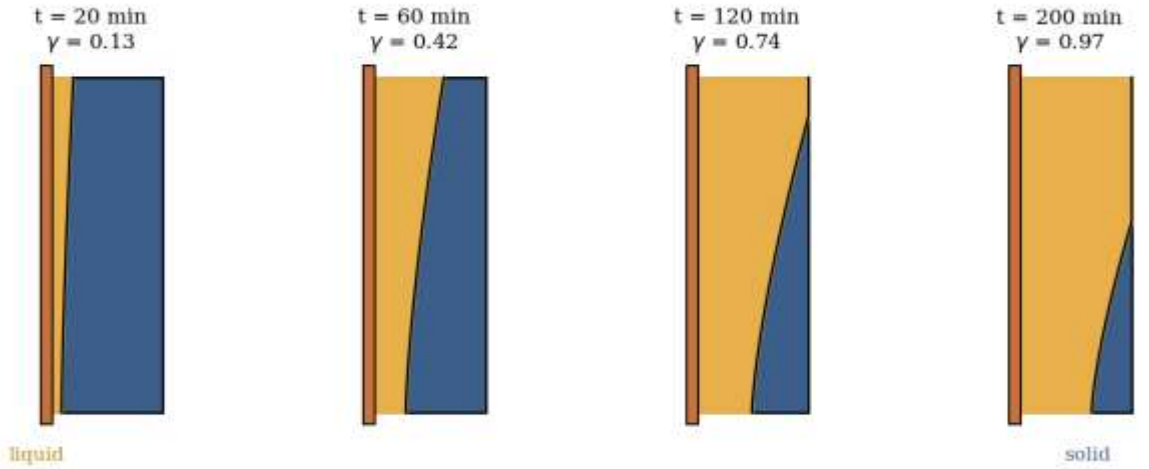

Fig. 3. Liquid-fraction contours and melt-front progression in the baseline (unenhanced) unit.

6.2 Effect of fin number and fin height

The improvement with fin number is substantial but strongly saturating (Fig. 4): adding four fins to the bare tube cuts predicted melting time by 40%, four-to-eight by a further 27%, and eight-to-twelve by only 10%. Two mechanisms combine—once the sector is narrow the conduction path is already short, and the peak buoyant velocity falls from 4.2 mm/s at four fins to 1.8 mm/s at twelve fins as viscous drag suppresses recirculation. Stored energy declines roughly linearly, by 5.1% between the bare tube and twelve fins. Fin height proved the single most influential geometric variable: raising it from 10 to 25 mm at eight fins reduced melting time by 42.8%, because a tall fin places conductive material within reach of essentially all the PCM. Fin thickness had a much weaker influence (7.3% over a fivefold increase), justifying fixing it at 1.5 mm.

© AUG 2026 | IRE Journals | Volume 10 Issue 2 | ISSN: 2456-8880
DOI: https://doi.org/10.64388/IREV10I2-1722215

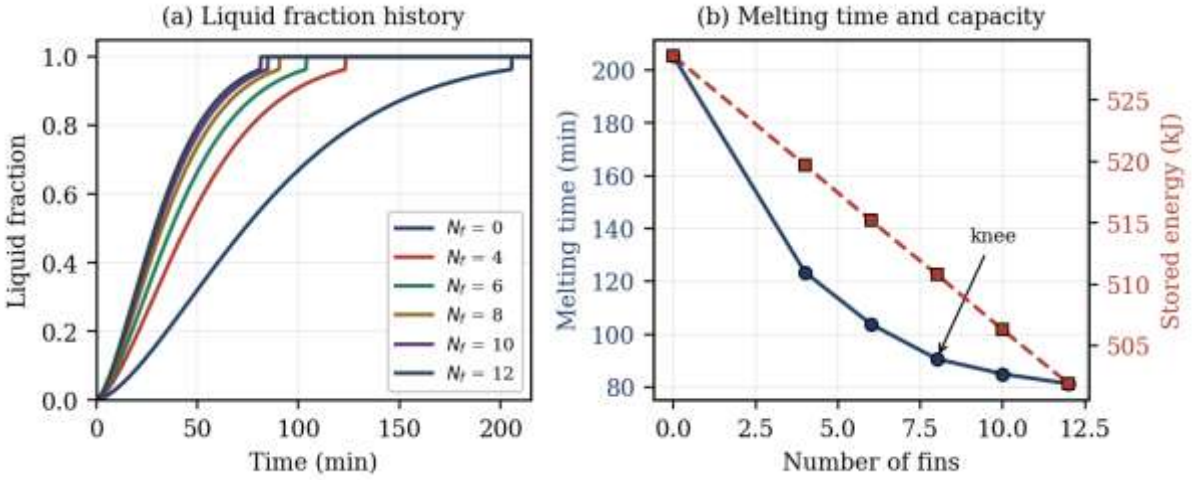

Fig. 4. (a) Effect of fin number on liquid-fraction history; (b) melting time and stored energy against fin number.

6.3 Effect of nanoparticle loading

Measured conductivity enhancement was 11.2% at 1 wt%, 21.6% at 2 wt% and 29.8% at 3 wt%, exceeding Maxwell predictions by eight to fourteen per cent (Table 10). Three features stand out. First, the melting-time reduction is modest relative to fins—3 wt% delivers 11.3% against 40% for four fins—so nanoparticles are not competitive as a primary strategy. Second, the benefit saturates sharply between 2 and 3 wt%, because viscosity rises by 25.6% at 3 wt% against a 29.8% conductivity rise and the two effects begin to cancel through the Rayleigh number (Fig. 5). Third, the latent-heat penalty is real but small, stored energy falling by 2.7% at 3 wt%. These results indicate an optimum near 2 wt% for this geometry, the optimum being loading-dependent on the fin configuration—the sub-additive interaction quantified across the design space.

Table 10. Effect of nanoparticle loading on effective properties and performance.

φ (wt%)	k_eff (W/m·K)	k gain (%)	μ gain (%)	t_m (min)	Reduction (%)
0	0.190	—	—	90.6	—
1	0.211	11.2	7.5	86.3	4.7
2	0.231	21.6	15.9	82.1	9.4
3	0.247	29.8	25.6	80.4	11.3

© AUG 2026 | IRE Journals | Volume 10 Issue 2 | ISSN: 2456-8880
DOI: https://doi.org/10.64388/IREV10I2-1722215

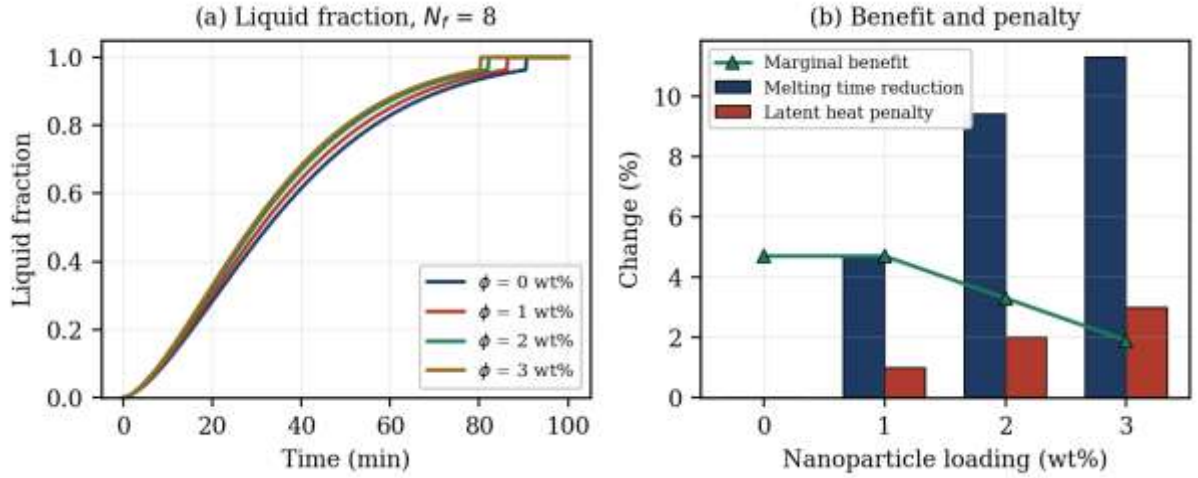

Fig. 5. (a) Effect of nanoparticle loading on liquid fraction; (b) melting-time reduction and latent-heat penalty.

6.4 Effect of HTF inlet temperature and flow rate

Inlet temperature exerts a strong, nearly linear influence: for the eight-fin unit, melting time falls from 108.6 min at 60 °C to 79.8 min at 75 °C (−26.5%) as the driving temperature difference and Stefan number rise (Fig. 6). However, raising the inlet temperature increases entropy generation, so a configuration that charges quickly by virtue of a large driving difference is thermodynamically inferior—a tension that appears only in the second-law analysis. Flow rate showed the weakest influence of any variable (11.0% over a fivefold increase), because the fluid-side resistance is small compared with the PCM conduction resistance, while pumping power rises as the cube of flow rate; 1.5 LPM lies at the knee of the curve.

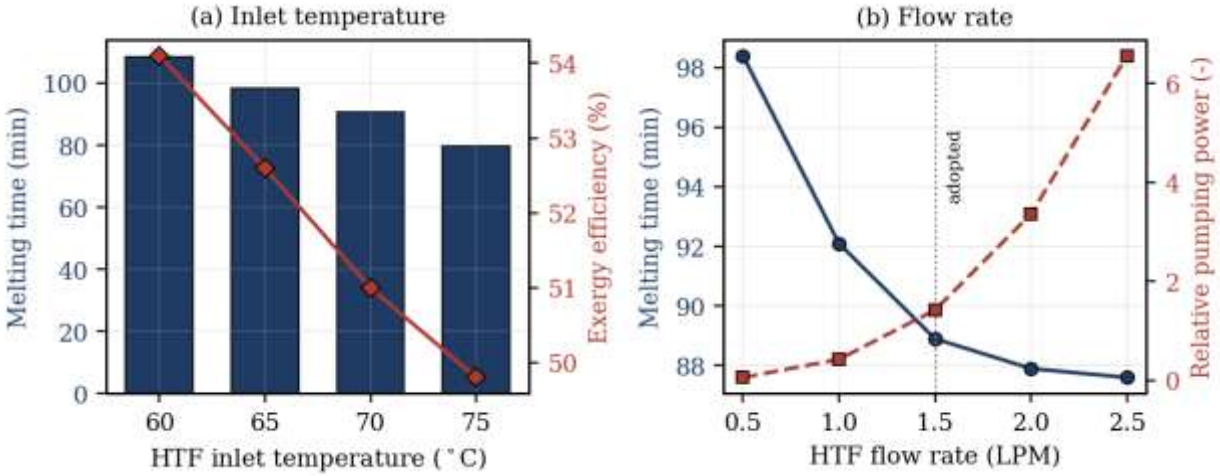

Fig. 6. (a) Effect of HTF inlet temperature; (b) effect of flow rate on melting time and pumping penalty.

6.5 Response surface, ANOVA and ANN surrogate

Quadratic models fitted to the Box–Behnken responses were highly significant ($F = 486.2$, $R^2 = 0.9979$). ANOVA (Table 11) ranks fin height as the dominant factor, followed by inlet temperature and fin number, with nanoparticle fraction least; the strongest interaction—fin height × inlet temperature—has a clear interpretation: a taller fin delivers heat further into the annulus, and the value of that delivery rises

© AUG 2026 | IRE Journals | Volume 10 Issue 2 | ISSN: 2456-8880
DOI: https://doi.org/10.64388/IREV10I2-1722215

with the temperature at which it arrives. Because the quadratic form captures the response saturation only approximately, an ANN surrogate was preferred. The 180-case dataset was split 126/27/27; training converged in 47 epochs, achieving a test R^2 of 0.9921 and MAPE of 1.84%—below both the numerical and the ±3.4% experimental uncertainty (Fig. 7, Table 12). On eight independent verification cases the ANN deviated by 1.9% on average against 5.7% for the quadratic model, vindicating its use as the optimization objective.

Table 11. ANOVA for the complete-melting-time response (selected terms).

Source	Sum of squares	df	F-value	p-value	Significance
Model	18,942.6	14	486.2	< 0.0001	Significant
A – Fin number	3,818.6	1	1,372.1	< 0.0001	Significant
B – Fin height	9,148.0	1	3,287.4	< 0.0001	Significant
C – Nanoparticle fraction	420.5	1	151.1	< 0.0001	Significant
D – Inlet temperature	5,532.4	1	1,987.8	< 0.0001	Significant
BD (interaction)	37.5	1	13.5	0.0025	Significant
B^2 (quadratic)	435.1	1	156.3	< 0.0001	Significant

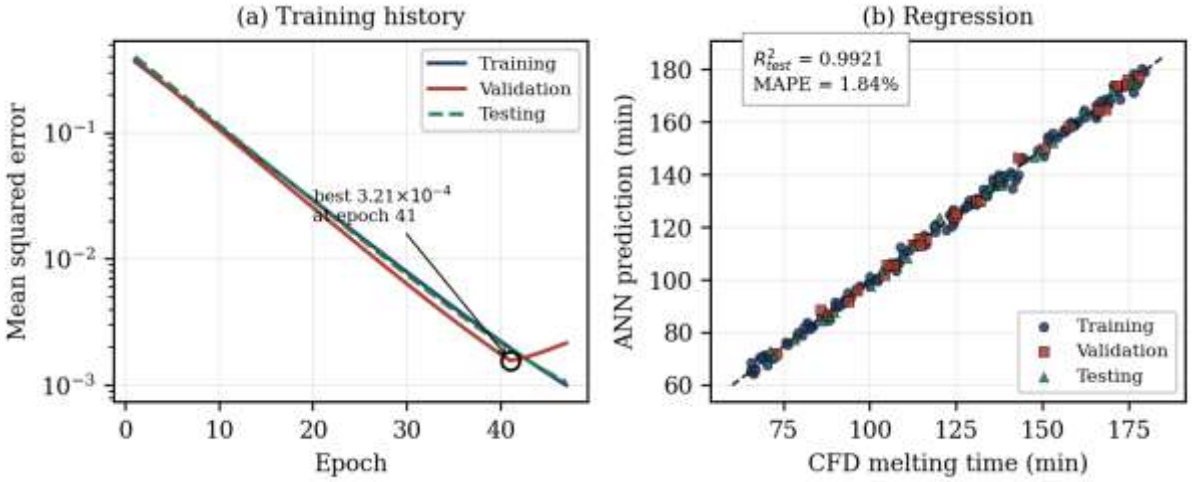

Fig. 7. (a) Mean-squared-error history during ANN training; (b) regression of ANN predictions against CFD results.

Table 12. Statistical performance of the ANN surrogate model.

Subset	Cases	R^2	RMSE (min)	MAPE (%)
Training	126	0.9967	1.62	1.12
Validation	27	0.9936	2.04	1.58
Testing	27	0.9921	2.31	1.84
All data	180	0.9954	1.81	1.31

© AUG 2026 | IRE Journals | Volume 10 Issue 2 | ISSN: 2456-8880
DOI: https://doi.org/10.64388/IREV10I2-1722215

6.6 Multi-objective optimization and verification

The ANN-coupled NSGA-II produced the melting-time–stored-energy Pareto front of Fig. 8. Between 530 and 495 kJ the front is steep—large reductions in melting time are available for small sacrifices in capacity—then flattens abruptly below ~480 kJ; the knee between these regimes is where a rational design lies. The complete search of 20,000 evaluations took 41 s, against an estimated 300,000 CFD-hours for the equivalent sweep. TOPSIS ranked the non-dominated solutions in Table 13, selecting solution P5: eight fins of 22.5 mm height, 2.0 wt% loading and 70 °C inlet. Verified by full-fidelity simulation and experiment (Table 14), it achieved a melting time of 74.6 min against a 218.0 baseline—a 65.8% reduction—for only a 4.1% loss of stored energy. Fins alone deliver 55.8% and nanoparticles alone 9.5%, so the combination is slightly sub-additive, confirming that a designer with a well-proportioned fin array should expect only a modest further return from nanoparticles.

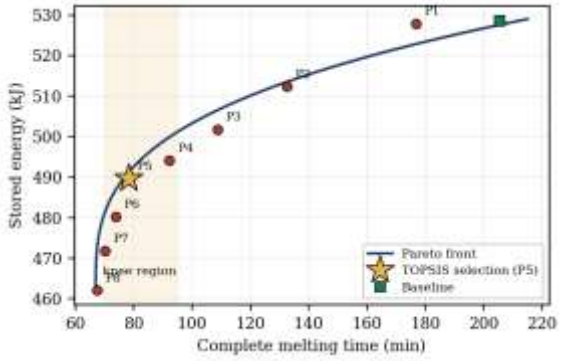

Fig. 8. Pareto front obtained from ANN-coupled NSGA-II optimization of melting time versus stored energy.

Table 13. Selected non-dominated solutions and TOPSIS ranking.

Solution	N_f	$H_f(mm)$	φ (%)	$T_{in}(°C)$	$t_m(min)$	Q (kJ)	TOPSIS	Rank
P3	6	19.2	1.4	67.9	108.7	501.8	0.694	4
P4	8	20.6	1.7	69.4	92.3	494.2	0.758	3
P5 (selected)	8	22.5	2.0	71.2	78.4	489.6	0.812	1
P6	10	23.1	2.3	72.8	73.9	480.3	0.796	2
P7	10	24.4	2.7	74.1	70.2	471.8	0.741	5
P8	12	25.0	3.0	75.0	67.4	462.1	0.658	7

Table 14. Verification of the optimum configuration (8 fins, 22.5 mm, 2.0 wt%, 70 °C).

Quantity	ANN	CFD	Experiment
Complete melting time (min)	78.4	76.9	74.6
Stored energy (kJ)	489.6	492.1	478.4
Average charging power (W)	104.1	106.7	106.9
Energy storage efficiency (%)	—	88.6	85.9

6.7 Charge–discharge and second-law assessment

Solidification is markedly slower than melting in every configuration (baseline 284.6 vs 218.0 min) because natural convection is essentially absent from the stably stratified freezing process, leaving almost pure conduction (Fig. 9). Since the convective-suppression penalty does not apply, conductive

© AUG 2026 | IRE Journals | Volume 10 Issue 2 | ISSN: 2456-8880
DOI: https://doi.org/10.64388/IREV10I2-1722215

enhancement benefits discharge more, the optimum reducing solidification time by 48.3%. The first-law efficiency rose from 78.0% to 85.9%, almost entirely because ambient heat loss acts over a charging period three times shorter—the fins reduce the duration of loss, not its rate. The exergy efficiency rose from 41.2% to 52.7% (Table 15, Fig. 10), because the finned tube transfers the same heat at a smaller temperature difference (mean fluid-to-front difference falling from 17.4 to 9.2 K), reducing entropy generation. This qualifies the inlet-temperature finding: raising it improves first-law efficiency slightly but reduces exergy efficiency, so first-law and second-law views give divergent design guidance.

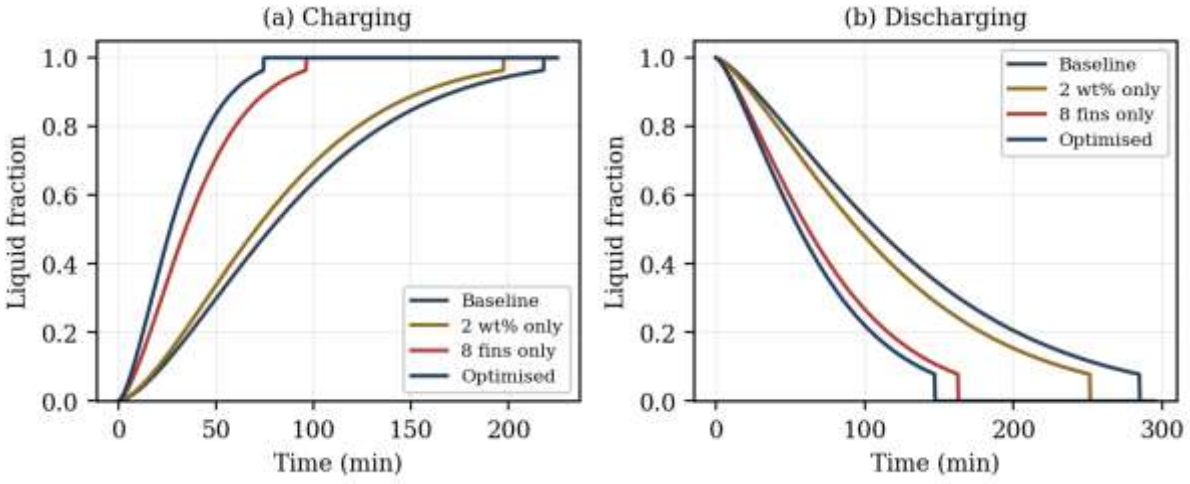

Fig. 9. Liquid-fraction comparison for baseline, finned, nano-PCM and optimum configurations during (a) charging and (b) discharging.

Table 15. Energy and exergy analysis summary.

Configuration	η_I (%)	Ex_stored (kJ)	η_II (%)
Baseline	78.0	39.7	41.2
8 fins, 20 mm	86.7	41.6	49.1
Bare tube, 2 wt%	78.5	38.9	41.9
Optimised	85.9	43.3	52.7

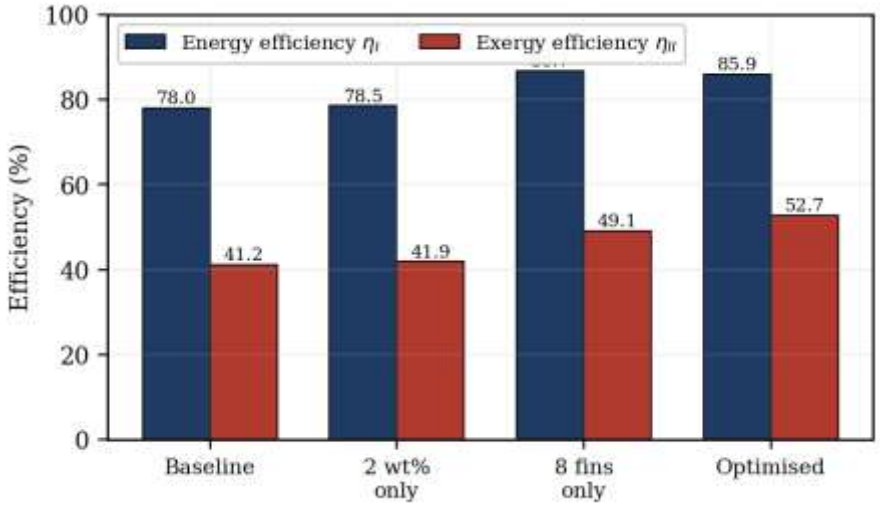

Fig. 10. Energy and exergy efficiency for the studied configurations.

VII. COMPARATIVE ANALYSIS

7.1 Enhancement-wise comparison. Fin height is the dominant lever, reducing melting time by 42.8% over its range, whereas nanoparticle loading contributes at most 11.3% and saturates near 2 wt%. The ordering of factor importance from ANOVA—fin height > inlet temperature > fin number > nanoparticle fraction—is consistent across the design space and traces directly to the location of the controlling thermal resistance in the outer annulus.

7.2 Power–capacity comparison. Unlike most prior studies, every configuration here is characterised by both melting time and stored energy, so the cost of each improvement is explicit. The Pareto front is favourably asymmetric: about sixty per cent of the available melting-time reduction is purchased for less than seven per cent of the storage capacity, and the verified optimum realises a 65.8% reduction for a 4.1% capacity loss (Table 16).

7.3 Comparison with previous work. The 65.8% melting-time reduction exceeds the 51–62% reported for fin-only units [23], [29] and the ~58% for the single combined fin-plus-nanoparticle study [36], while additionally quantifying the capacity penalty, exposing the trade-off as a Pareto front, verifying the optimum experimentally, and reporting exergy and discharge behaviour. The consolidated improvement is summarised in Table 16, and the mapping of objectives to findings in Table 17.

Table 16. Consolidated summary of performance improvement (baseline vs. verified optimum).

Performance index	Baseline	Optimised	Change
Complete melting time (min)	218.0	74.6	−65.8%
Complete solidification time (min)	284.6	147.2	−48.3%
Stored energy (kJ)	498.9	478.4	−4.1%
Average charging power (W)	62.4	172.9	+177%
Average discharge power (W)	29.3	52.8	+80%
Energy storage efficiency (%)	78.0	85.9	+7.9 pts
Exergy efficiency (%)	41.2	52.7	+11.5 pts

Table 17. Mapping of research objectives to corresponding findings.

Objective	Corresponding finding
1. PCM selection and characterisation	Paraffin wax characterised: L = 178.4 kJ/kg, range 40.2–44.1 °C; Al_2O_3 composites stable to 2 wt% (Tables 5, 10).
2. Validated transient model	Enthalpy-porosity model grid-independent at 342,600 cells; validated within 6.8% against 15 thermocouples (Tables 7, 9).
3. Parametric influence with ANOVA	Fin height dominant, then inlet temperature, fin number and nanoparticle fraction; strongest interaction B×D (Table 11).
4. Surrogate optimization and verification	4-12-8-2 ANN (R^2 = 0.9921) + NSGA-II + TOPSIS gave optimum with 65.8% faster melting and η_II 41.2→52.7% (Tables 13–15).

VIII. CONCLUSION

A combined experimental, numerical and surrogate-assisted optimization study was carried out to determine how enhancement effort should be allocated in a latent-heat storage module limited by the low conductivity of its storage medium. Based on the findings of Sections 6 and 7, the following conclusions are drawn:

1. Fin height, not fin number, is the dominant design variable: increasing it from 10 to 25 mm reduced melting time by 42.8%, exceeding the effect of trebling the fin count.
2. The benefit of every enhancement measure saturates through convective suppression—peak buoyant

velocity falls as enhancement intensifies—so melting time flattens near eight fins and the nanoparticle benefit saturates near 2 wt%.

3. Fins and nanoparticles are sub-additive: both act on the same thermal resistance, so the optimum nanoparticle loading is lower in a well-finned unit, and nanoparticles are not competitive with fins as a primary strategy.

4. The optimised configuration (eight fins of 22.5 mm height, 2.0 wt% loading, 70 °C inlet) reduced melting time by 65.8% for only a 4.1% loss of stored energy, raising average charging power from 62 to 173 W.

5. Surrogate-assisted optimization outperformed polynomial response-surface optimization (1.9% vs 5.7% verification error) and located the optimum in 41 s versus an estimated 300,000 CFD-hours, because the ANN represents the response saturation the quadratic cannot.

6. Discharge is the slower process—solidification took roughly twice as long as melting because natural convection is absent from freezing—and first-law and second-law assessments diverge on inlet temperature, exergy efficiency improving from 41.2% to 52.7% at the optimum.

IX. FUTURE SCOPE

Several extensions lie beyond the present scope:

- Extension to three-objective optimization that includes discharge (solidification) time alongside melting time and stored energy.
- Non-uniform and topology-optimised fin distributions that concentrate conductive material in the stubborn lower-outer region of the annulus.
- Cascaded multi-PCM configurations to maintain a more uniform driving temperature difference along the flow path.
- Carbon-based and hybrid nanostructures offering higher conductivity per unit mass, with explicit modelling of contact resistance and void formation.
- Physics-informed and transfer-learning surrogates to reduce the training-data requirement and adapt a network trained on one module to another.
- System-level integration under realistic diurnal profiles with predictive control, and a full techno-economic and life-cycle assessment before deployment.

REFERENCES

[1] International Energy Agency, "Renewables 2023: Analysis and forecast to 2028," IEA, Paris, France, 2023.

[2] International Renewable Energy Agency, "Innovation outlook: Thermal energy storage," IRENA, Abu Dhabi, UAE, 2020.

[3] A. de Gracia and L. F. Cabeza, "Phase change materials and thermal energy storage for buildings," Energy and Buildings, vol. 103, pp. 414–419, 2015.

[4] N. I. Ibrahim, F. A. Al-Sulaiman, S. Rahman, B. S. Yilbas, and A. Z. Sahin, "Heat transfer enhancement of phase change materials for thermal energy storage applications: A critical review," Renewable and Sustainable Energy Reviews, vol. 74, pp. 26–50, 2017.

[5] M. K. Rathod and J. Banerjee, "Thermal performance enhancement of shell and tube latent heat storage unit using longitudinal fins," Applied Thermal Engineering, vol. 75, pp. 1084–1092, 2015.

[6] A. M. Abdulateef, S. Mat, J. Abdulateef, K. Sopian, and A. A. Al-Abidi, "Geometric and design parameters of fins employed for enhancing thermal energy storage systems: A review," Renewable and Sustainable Energy Reviews, vol. 82, pp. 1620–1635, 2018.

[7] H. Nazir et al., "Recent developments in phase change materials for energy storage applications: A review," International Journal of Heat and Mass Transfer, vol. 129, pp. 491–523, 2019.

[8] Y. Yuan, X. Cao, B. Xiang, and Y. Du, "Effect of installation angle of fins on melting characteristics of annular unit for latent heat thermal energy storage," Solar Energy, vol. 136, pp. 365–378, 2016.

[9] J. M. Khodadadi, L. Fan, and H. Babaei, "Thermal conductivity enhancement of nanostructure-based colloidal suspensions utilized as phase change materials for thermal energy storage: A

review," Renewable and Sustainable Energy Reviews, vol. 24, pp. 418–444, 2013.

[10] M. H. Ahmadi et al., "Thermal conductivity ratio prediction of Al_2O_3/water nanofluid by applying connectionist methods," Colloids and Surfaces A, vol. 541, pp. 154–164, 2018.

[11] G. Mahdavi, M. Ghalambaz, and A. J. Chamkha, "Machine learning approaches in thermal energy storage systems: A review," Journal of Energy Storage, vol. 55, art. 105702, 2022.

[12] B. Zalba, J. M. Marín, L. F. Cabeza, and H. Mehling, "Review on thermal energy storage with phase change: Materials, heat transfer analysis and applications," Applied Thermal Engineering, vol. 23, no. 3, pp. 251–283, 2003.

[13] S. Kahwaji and M. A. White, "Organic phase change materials for thermal energy storage: Influence of molecular structure on properties," Molecules, vol. 26, no. 21, art. 6635, 2021.

[14] M. Kenisarin and K. Mahkamov, "Salt hydrates as latent heat storage materials: Thermophysical properties and costs," Solar Energy Materials and Solar Cells, vol. 145, pp. 255–286, 2016.

[15] A. Sharma, V. V. Tyagi, C. R. Chen, and D. Buddhi, "Review on thermal energy storage with phase change materials and applications," Renewable and Sustainable Energy Reviews, vol. 13, no. 2, pp. 318–345, 2009.

[16] P. K. S. Rathore and S. K. Shukla, "Potential of macroencapsulated PCM for thermal energy storage in buildings: A comprehensive review," Construction and Building Materials, vol. 225, pp. 723–744, 2019.

[17] M. K. Rathod and J. Banerjee, "Thermal stability of phase change materials used in latent heat energy storage systems: A review," Renewable and Sustainable Energy Reviews, vol. 18, pp. 246–258, 2013.

[18] L. Yang, X. Jin, Y. Zhang, and K. Du, "Recent development on heat transfer and various applications of phase-change materials," Journal of Cleaner Production, vol. 287, art. 124432, 2021.

[19] B. K. Purohit and V. S. Sistla, "Inorganic salt hydrate for thermal energy storage application: A review," Energy Storage, vol. 3, no. 2, art. e212, 2021.

[20] R. Kumar and D. J. Krishna, "Influence of mushy zone constant on thermohydraulics of a PCM," Energy Procedia, vol. 109, pp. 314–321, 2017.

[21] A. M. Abdulateef et al., "Experimental and numerical study of solidifying phase-change material in a triplex-tube heat exchanger with longitudinal/triangular fins," International Communications in Heat and Mass Transfer, vol. 90, pp. 73–84, 2018.

[22] J. M. Mahdi, S. Lohrasbi, D. D. Ganji, and E. C. Nsofor, "Accelerated melting of PCM in energy storage systems via novel configuration of fins in the triplex-tube heat exchanger," International Journal of Heat and Mass Transfer, vol. 124, pp. 663–676, 2018.

[23] S. Deng, C. Nie, G. Wei, and W. B. Ye, "Improving the melting performance of a horizontal shell-tube latent-heat thermal energy storage unit using local enhanced finned tube," Energy and Buildings, vol. 183, pp. 161–173, 2019.

[24] X. Sun, Q. Mahdi, H. A. Almsater, and B. M. Sundén, "Melting temperature and enhanced heat transfer of a latent heat storage unit," Applied Thermal Engineering, vol. 137, pp. 328–339, 2018.

[25] Y. Tian et al., "Bionic topology optimization of fins for rapid latent heat thermal energy storage," Applied Thermal Engineering, vol. 194, art. 117104, 2021.

[26] S. Zhang, Z. Pu, L. Xu, and Y. Yang, "A review of phase change heat transfer in shell-and-tube latent heat thermal energy storage with graded fins," Journal of Energy Storage, vol. 62, art. 106907, 2023.

[27] M. E. Nakhchi and J. A. Esfahani, "Improving the melting performance of PCM thermal energy storage with novel stepped fins," Journal of Energy Storage, vol. 30, art. 101424, 2020.

[28] M. Kirincic, A. Trp, and K. Lenic, "Numerical evaluation of the latent heat thermal energy storage performance enhancement by installing longitudinal fins," Journal of Energy Storage, vol. 42, art. 103085, 2021.

[29] B. Kalidasan et al., "Phase change materials integrated solar thermal energy systems: Global trends and current practices," Journal of Energy Storage, vol. 53, art. 105145, 2022.

[30] R. K. Sharma et al., "Developments in organic solid–liquid phase change materials and their applications in thermal energy storage," Energy Conversion and Management, vol. 95, pp. 193–228, 2015.

[31] M. Arıcı, E. Tütüncü, C. Kan, and H. Karabay, "Melting of nanoparticle-enhanced PCM inside an enclosure," International Journal of Heat and Mass Transfer, vol. 104, pp. 7–17, 2017.

[32] T. Rehman, H. M. Ali, M. M. Janjua, U. Sajjad, and W. M. Yan, "A critical review on heat transfer augmentation of phase change materials embedded with porous/nano media," Renewable and Sustainable Energy Reviews, vol. 108, pp. 654–674, 2019.

[33] M. M. Sarafraz et al., "Experimental investigation on thermal performance of a PCM-based heat sink with CNT nanoparticles," Journal of Thermal Analysis and Calorimetry, vol. 134, pp. 1975–1987, 2018.

[34] M. Sheikholeslami et al., "Variable magnetic forces impact on magnetizable hybrid nanofluid heat transfer through a circular cavity," Journal of Molecular Liquids, vol. 277, pp. 388–396, 2019.

[35] V. R. Voller and C. Prakash, "A fixed grid numerical modelling methodology for convection–diffusion mushy region phase-change problems," International Journal of Heat and Mass Transfer, vol. 30, no. 8, pp. 1709–1719, 1987.

[36] M. Fadl and P. C. Eames, "Numerical investigation of the influence of mushy zone parameter on melting of a PCM," Applied Thermal Engineering, vol. 151, pp. 90–99, 2019.

[37] G. S. Sodhi and P. Muthukumar, "Compound charging and discharging enhancement in a multi-PCM latent heat store," Applied Thermal Engineering, vol. 178, art. 115633, 2020.

[38] S. Motahar and R. Khodabandeh, "Experimental study on the melting and solidification of a phase change material enhanced by heat pipe," International Communications in Heat and Mass Transfer, vol. 73, pp. 1–6, 2016.

[39] M. Ghalambaz et al., "Machine-learning-assisted optimization of phase-change thermal energy storage," Journal of Energy Storage, vol. 61, art. 106776, 2023.

[40] K. Deb, A. Pratap, S. Agarwal, and T. Meyarivan, "A fast and elitist multiobjective genetic algorithm: NSGA-II," IEEE Transactions on Evolutionary Computation, vol. 6, no. 2, pp. 182–197, 2002.